Experimental observations of thermo-optical bistability and self-pulsation in silicon microring resonators

Libin Zhang, Yonghao Fei, Yanmei Cao, Xun Lei, and Shaowu Chen*

State Key Laboratory on Integrated Optoelectronics, Institute of Semiconductors, Chinese Academy of Sciences, Beijing 100083, China *Corresponding author: swchen@semi.ac.cn

Received September 17, 2013; revised November 18, 2013; accepted November 29, 2013; posted December 2, 2013 (Doc. ID 197890); published January 6, 2014

Optical bistability and self-pulsation (SP) in silicon microring resonators (MRRs) are experimentally observed. The waveforms and frequencies of SP can be controlled by changing input light power and its wavelength, and the region of SP can be modulated readily by applying a reverse voltage on the PN junction embedded in the MRR. These phenomena are theoretically studied by adopting the coupled-mode theory and linear stability analysis method for differential equations, with theoretical results fitting well with the experimental ones. © 2014 Optical Society of America

OCIS codes: (190.1450) Bistability; (190.3100) Instabilities and chaos; (190.4390) Nonlinear optics, integrated optics; (230.4555) Coupled resonators. http://dx.doi.org/10.1364/JOSAB.31.000201

1. INTRODUCTION

Silicon microring resonators (MRRs) have shown great potential applications in passive as well as active photonic devices. The needs for low power consumption and high integration density result in an unprecedented reduction in the footprint of waveguide devices and radius of MRRs. As a result, the power used to stimulate nonlinear phenomena in silicon MRRs, especially optical bistability (BI) and self-pulsation (SP), has been reduced to less than 1 mW, as demonstrated by some reported experiments employing etched and etchless MRRs [1–3]. The other generally used structures for studying thermo-optical (TO) phenomenon are silicon microdisks or microtoroids, with only $35 \,\mu W$ and $480 \,\mu W$ needed to stimulate BI and SP, respectively [4]. In silicon MRRs, three key characteristic times-photon lifetime, free-carrier lifetime, and thermal decay time—affect the dynamical process of the optical field evolution within the MRRs. We have theoretically studied the nonlinear phenomena in silicon MRRs in two situations with and without considering the TO effect [5,6]. Both BI and SP can be observed in these two cases, however, with different nonlinear behavior regions and SP frequencies. Although some reported works based on Kerr whispering gallery mode resonators, such as silica microtoroid or microsphere, have shown TO dynamical pulsation as well [7,8], such processes are much more complicated than that in the silicon MRRs, due to the different intrinsic nonlinear effects, thus being hard to control and their potential applications being limited.

In this work, the BI and SP in silicon MRRs which are fabricated by CMOS process are experimentally studied. By employing the mathematical model we have presented in our previous work [6], the theoretical results are given, which fit well with the experimental measurements, thus consolidating the validity of our theoretical model. However, the SP phenomenon is not observed in experiment when applying a

reverse voltage on the PN junction embedded in the MRR, which is also discussed with the model. The article is organized as follows: in Section 2, the experimental setup and results are described. In Section 3, the comparison of the experimental measurements with our model and a discussion are given. Finally, a conclusion is presented.

2. EXPERIMENTAL SETUP AND RESULTS

Figure $\underline{\mathbf{1}}$ shows the schematic of the measurement setup. A tunable continuous-wave laser is amplified by an erbium-doped fiber amplifier (EDFA) and then is polarized by a polarization controller (PC). Before the light has been coupled into the waveguide of silicon MRR, an optical tunable power attenuator is used to adjust the light power. At both facets of the waveguide chip, two tapered fibers are used to couple the light into and out of the waveguide respectively. The outcoming light is then split into two parts by a splitter with one part fed into an optical spectrum analyzer (OSA) and the other into an oscilloscope via a photodetector (PD) to test the real-time waveforms.

The scanning electron microscope (SEM) image of the MRR used in the experiment is shown in the inset of Fig. $\underline{1}.$ The whole device consists of a ring resonator with a radius of $10~\mu m$ side-coupled with a bus waveguide and a PN junction, which is embedded in the ring waveguide and terminated with a three-port electrode, thus making it possible to control the carrier density and carrier lifetime in the ring waveguide by applying outside voltage. The carriers concentration distribution in the waveguide is similar to those in the published paper [9] where the same CMOS process was adopted, that in the range of $10^{17}~cm^{-3}.$ After ion implantation, a high temperature process is adopted to activate the dopant in $1030^{\circ}C$ for 5~s. The waveguides adopted in our experiment is rib ones etched on a SOI wafer with the inner rib height of 220~nm, outside slab height of 60~nm, and strip width of 500~nm.

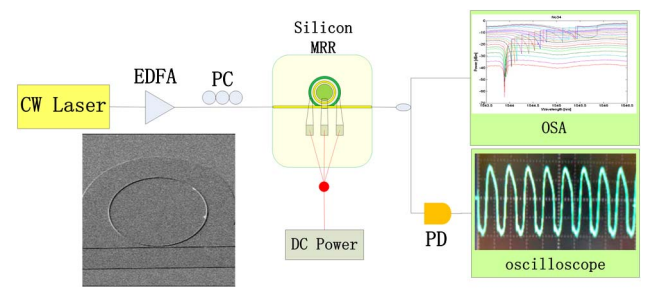


Fig. 1. Schematic of the measurement setup. The laser is amplified by EDFA and its polarization is controlled by PC, single-mode tapered fiber is used to couple the light into and out of the chip with coupling loss of about 5 dB/facet. A DC power is used to adjust the free-carrier lifetime. Inset: SEM image of silicon MRR before fabricated PN junction. CW laser, tunable continuous-wave laser; EDFA, erbium-doped fiber amplifier; PC, polarization controller; PD, photodetector; OSA, optical spectrum analyzer.

The gap between the ring waveguide and the bus waveguide is about 250 nm. Such waveguide can only support TE mode, and the measured transmitted optical spectrum at different input power is plotted in Fig. 2. The linear resonant wavelength is 1543.89 nm and the extinction ratio is larger than 25 dB. The 3 dB width of the spectrum is about 80 pm, which corresponds to a loaded quality factor about 20,000. Such MRR is nearly working under the critical coupling condition where the linear loss nearly equals to the coupling loss. The intrinsic quality factor is about 40,000, indicating the ring linear loss and coupling loss both equal to 4 cm⁻¹.

Due to the TO effect, the resonant wavelength is redshifted when the input power increases. It is known that in silicon waveguides the free-carrier dispersion (FCD) effect also plays an important role in changing the refractive index, which makes the resonant wavelength blueshifting. For example, some articles have experimentally shown that the resonant wavelength is blueshifted with increasing the input power at the beginning stage, especially in case of the etchless MRRs or under extremely low temperature [3,10]. However, in our silicon MRR, although the waveguide is doped so that the free-carrier lifetime is shorter than that in the etchless ones,

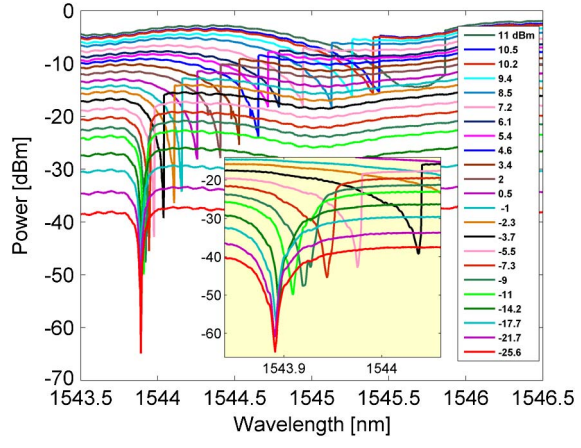


Fig. 2. Measured spectra of optical transmission of the silicon MRR (without GSG probe) at various input power levels. The quoted input power refers to the power at the bus waveguide before coupling into the MRR. Inset: zoom-in views of optical spectra for lower input powers. The laser wavelength is swept from shorter wavelength to longer wavelength.

the utilization of heavily doped slab waveguide and metal electrodes can greatly shorten the thermal decay time. As a result, TO plays a little larger yet still comparable role on the refractive index than FCD, which makes both BI and SP occur in the wavelength range blueshifted from the resonance of the MRR.

The threshold power of the BI state is measured to be about -7.3 dBm as seen in the inset of Fig. 2. This power is very low for a highly doped silicon MRR, which may broaden the application area of silicon MRR, such as an optical switch based on the BI. However, it is undesired in some wavelengthdependent applications, such as optical wavelength-division multiplexing devices and electro-optical high-speed switches, as a little higher power may redshift the resonant wavelength and destroy the preset match between input wavelength and ring resonant wavelength. Another phenomenon, i.e., optical SP, may be aroused when increasing the input power higher than several milliwatts, as can be seen in Fig. 3. With the help of a PD and a real-time oscilloscope, the oscillating waveforms of output light are observed. It is important to note that different input wavelengths have different optical oscillating waveforms. However, such dynamical process cannot be displayed in the optical spectra, as the power measured by an OSA is actually a mean power over a period of time that is much longer than the SP period time.

For a conventional silicon MRR without PN or PIN junction, the main characteristic times are normally constants. In this case, the region of SP, as well as the oscillating waveform and frequency, are all restricted by both input power and input wavelength. It is easy to control the SP through input light, which can be seen in Fig. 3. Furthermore, we measure the waveforms of output light at different input wavelengths with input power fixed at 8, 9, 10, and 11 dBm, respectively. The frequency and duty ratio of SP at different input wavelength detunings are plotted in Fig. 4 where the frequency of SP can be adjusted from 10 to 18 MHz. The maximum SP frequency appears at the middle of the region where the duty ratio of the waveform is near 0.5. Different from the trend of the "frequency-wavelength detuning" curve, the duty ratio decreases gradually with the increasing of the wavelength detuning, and its values can be adjusted almost from 1 to 0. Such phenomenon can be observed only when we sweep the input light from short wavelength to long wavelength by means of recording the real-time waveforms, which can hardly be observed with the opposite wavelength sweeping direction. The tunability of the SP as well as the relatively wide "0 to 1" duty ratio may provide some valuable flexibility in various potential applications.

3. THEORETICAL ANALYSIS AND DISCUSSION

The physical model has been proposed in [6] where the nonlinear coupled-mode theory (CMT) [11–14] and the linear stability analysis method [5,15,16] are used to simulate the dynamical process and predict the regions of BI and SP. In this paper, we only list some parameter values in Table 1, while other parameter values used in the model can be found in [6]. Some notes should be paid attention to, one is n_0 , which means group index; the other is η_{FCA} , which means how much power transforms to heat due to free-carrier absorption (FCA). The free-carrier lifetime used is 3 ns, which we attribute to the low loss of Si-SiO₂ interface. Two-photon

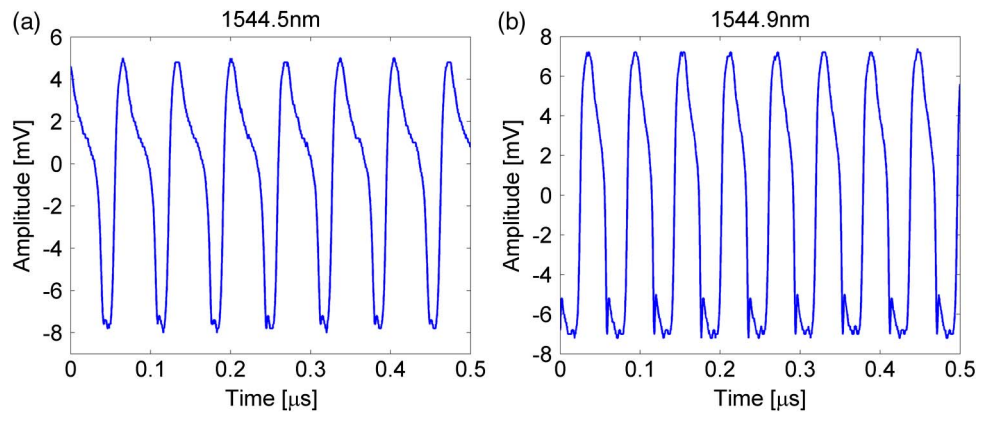


Fig. 3. Real-time waveforms at different input wavelength with fixed input power 10 dBm. (a) $\lambda = 1544.5$ nm ($\Delta\lambda = 610$ pm); (b) $\lambda = 1544.9$ nm ($\Delta\lambda = 1010$ pm). The movie of the dynamical process when sweeping the input wavelength from short to long can be found by clicking the hyperlink (Media 1).

absorption (TPA) induced free carriers in the waveguide are quickly separated by the build-in field of the PN junction, and thereafter a new balance of the free-carrier movement is built inside the waveguide. As a result, the recombination of carriers is mainly limited by the $\operatorname{Si-SiO}_2$ interface quality. The expression for the carrier lifetime in the waveguide, with the bulk carrier lifetime, Auger lifetime and carrier diffusion all ignored, is thus written as [17,18]

$$\frac{1}{\tau_{\rm car}} = \frac{S}{H} + \frac{W + 2(H - h)}{WH} S', \tag{1}$$

where W=500 nm, H=220 nm, h=60 nm, represent waveguide width and height, and the slab height, respectively. S and S' are the Si-SiO $_2$ interface recombination velocities in lower and upper interfaces, respectively. It is reported that such recombination velocity is influenced by the surface quality, and the values are 10^3-10^4 cm/s for common interface [19]. Compared with the values 8×10^3 cm/s used in [17] and considering the better quality of Si-SiO $_2$ interface in our case, we use 2.8×10^3 cm/s in simulations. Thus, the free-carrier lifetime is calculated to be 3 ns.

The theoretical boundaries of BI and SP are shown in Fig. 5, with the experimental measurements shown in black circles for comparison. The experimental BI boundary points fit well with the lower power branch of the theoretical BI boundary,

where the sweep direction of input wavelength is the same as in experiment, i.e., from short wavelength to long wavelength. However, when the operating wavelength is swept in the opposite direction, the boundary of BI takes its higher power branch. The OSA used in experiment can only support the sweeping direction from short wavelength to long wavelength, thus we only obtained the optical spectrum corresponding to the lower BI branch. To determine the higher power branch, an alternative method was used by sweeping input power from lower to higher while fixing the input wavelength. The critical power at the upper branch can be determined when the output power has a sharp jumping, as shown in Fig. 6(b). The measured power points were plotted in Fig. 6(a) (black circles), where the lower BI branch was also obtained by tuning the input power in the opposite direction (red rectangles). Considering the measured errors, the fitting between experimental data and predicted curves are acceptable.

Besides, the last measured point where wavelength detuning is about 2000 pm is a little far away from the theoretical value. The optical spectrum of this case is shown in Fig. $\underline{2}$ with the input power of 11 dBm, which is much different from other spectra. When the input power increases from 10.5 to 11 dBm, the linewidth of the resonance of the MRR broadens wider abruptly. To our knowledge, such phenomenon is not reported so far, and we guess it may have contributed to the additional optical loss and additional refractive index change

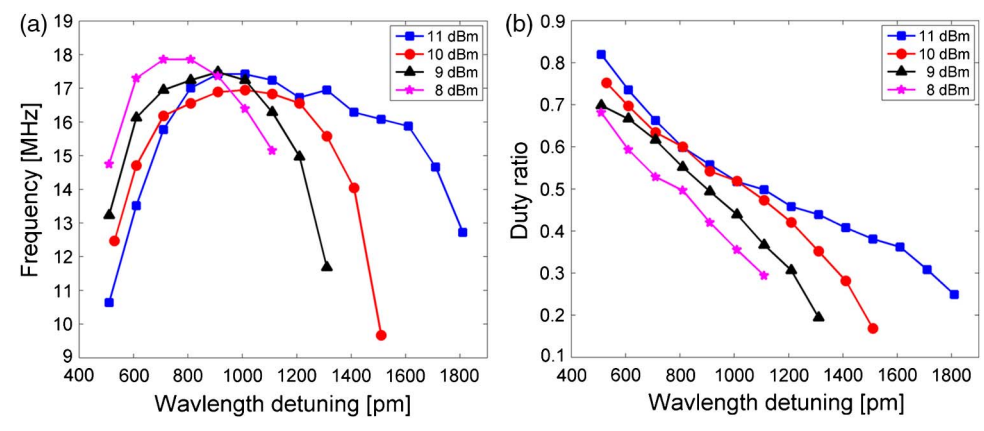


Fig. 4. (a) Frequency of output oscillation with input wavelength detuning at different input power. (b) Duty ratio of output oscillating waveforms with input wavelength detuning at different input power. The input power is 8, 9, 10, and 11 dBm, respectively.

Table 1. Parameter Values Used in Calculation

Parameter	Without Probe	With Probe -1 V	Source
Group index n_0	4	4	FimmWave
			[20]
Ring linear loss $\alpha_{\rm ring}$ (cm ⁻¹)	4	3.4	Measured
Coupling loss α_c (cm ⁻¹)	4	4	Measured
Free-carrier lifetime τ_{car} (ns)	3	0.03	Fit
Thermal decay time τ_{th} (μs)	0.12	0.12	Fit
$\eta_{ m lin}$	0.4	0.35	Fit
$\eta_{ ext{FCA}}$	0.9	0.9	Fit
$A_{\rm eff}~(\times 10^{-13}~{\rm m}^2)$	1.93	1.93	FimmWave
			[20]
$A_{\rm TPA}~(\times 10^{-13}~{\rm m}^2)$	1.1	1.1	Calculated
$A_{\rm FCA}~(\times 10^{-13}~{\rm m}^2)$	1.1	1.1	Calculated

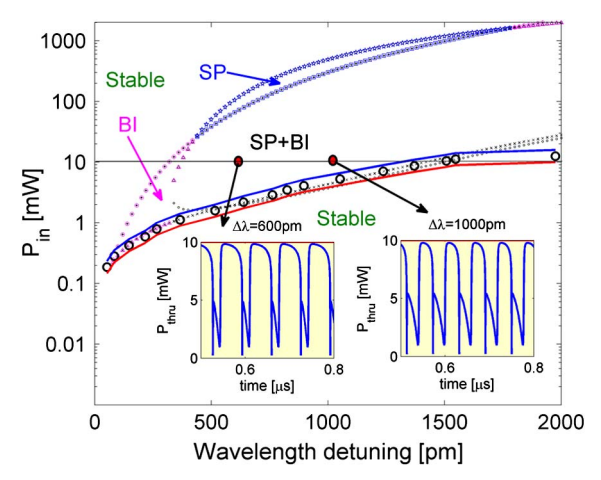


Fig. 5. Theoretical predicted boundaries of BI and SP at the map of input power and input wavelength detuning. The black circles denote the measured BI boundaries with the upper and lower solid lines representing the 1 dB power measurement tolerance. Insets: the numerical solutions of the used model showing the output dynamical waveforms at different input wavelength detunings with fixed input power at $10\ \mathrm{mW}.$ The wavelength detuning is $600\ \mathrm{and}\ 1000\ \mathrm{pm},$ respectively, which is marked by red circles.

of cladding silica under high light intensity. The nonlinear coefficient of silica is much smaller than that of silicon and can be neglected in most cases as long as the light intensity is not very high. However, it should be considered in the model whenever the light intensity in cladding is extremely high. As a result, the 3 dB resonance bandwidth is widely broadened and the resonant wavelength is largely redshifted.

Examples of output oscillating waveforms are shown in the insets of Fig. 5, with input power fixed at 10 dBm and input wavelength detuning at 600 and 1000 pm, respectively. Numerical results show that different input wavelength detunings have different waveforms, which is similar to the experimental measurements in Fig. 3. A more explicit relationship between frequency and input wavelength, together with the relationship between duty ratio and input wavelength are both plotted in Fig. 7. Comparing the experimental and theoretical output waveforms, it is found that as a whole they have the same trends and similar values. Nevertheless, there still exists a little difference between them and it may come from the imperfection of the model adopted, which ignores the counterpropagation of light coming from the waveguide sidewall scattering [4].

Furthermore, we have also studied the performance of a silicon MRR when applying a reverse biased voltage on the embedded PN junction and only the optical bistability can be observed, as seen in Fig. 8. The reverse voltage, together with the build-in voltage of the PN junction, sweep the free carriers out of the optical waveguide very quickly, resulting in a much shorter free-carrier lifetime [21] and a smaller linear loss due to the FCA. As a result, the extinction ratio of the resonance in the linear range is decreased, and the balance between the FCD and TO effects is broken. The role of the FCD on the refractive index is so much suppressed that the initial condition for SP cannot be satisfied, thus we can no longer observe the output power oscillation. The theoretical boundaries of BI are plotted in Fig. 8, where the carrier lifetime adopted is merely 30 ps, which is much shorter than that without electric probes onto the electrodes of the MRR. The lower power branch of the theoretical BI boundaries is in good agreement with the experimental measured data for the BI boundary. Note that some parameter values are also listed in Table 1.

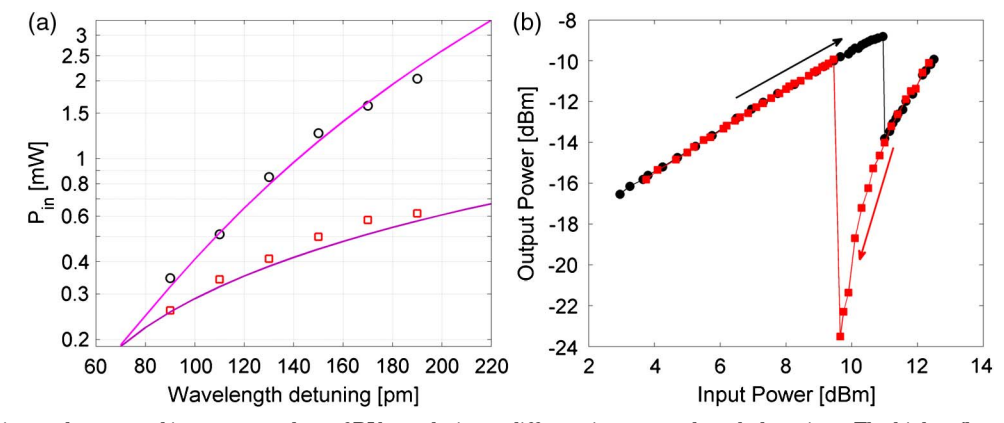


Fig. 6. (a) Experimental measured input power data of BI boundaries at different input wavelength detunings. The higher (lower) BI branch points marked by black circles (red rectangles) were measured by increasing (decreasing) the input power gradually. Two solid curves are the predicted BI boundaries. (b) One example of the relationship between output power and input power. Black: for input power increasing from lower to higher; Red: for input power decreasing from higher to lower. The power in horizontal and vertical coordinates has not excluded additional optical losses induced by couplers and polarization controller.

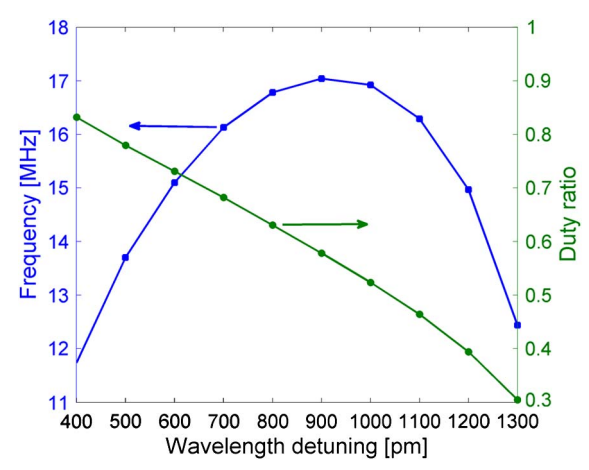
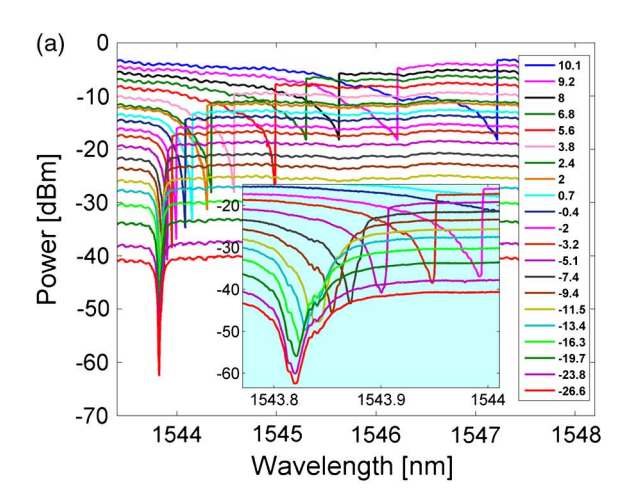


Fig. 7. Frequency and duty ratio of SP versus input wavelength detuning with input power fixed at 10 mW.

4. CONCLUSION

In this work we have experimentally observed the BI and SP phenomena in a highly doped silicon MRR. With the CMT and the linear stability analysis method, the experimental



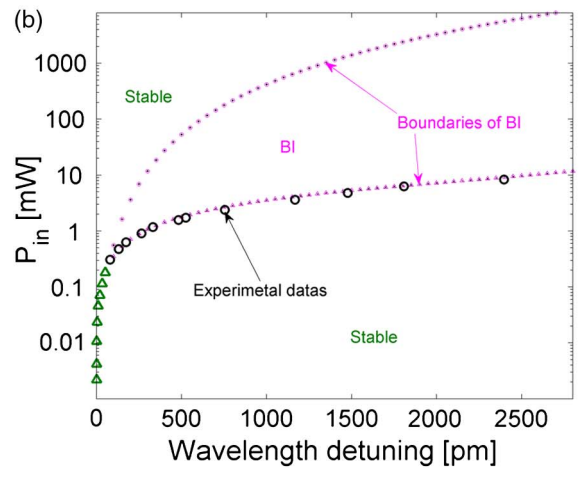


Fig. 8. (a) Experimental results of optical spectra at different input power with reverse voltage of –1 V. Inset: Zoom-in views of the spectra at lower input power. (b) Comparison between the experimental measurements (black circles and green triangles) and numerical results of the regions of BI (two pink-dotted lines). The green triangles mark the resonant wavelength before stimulating BI, while the black circles denote the BI boundary wavelength.

measurements, including the regions of BI and SP, and the real-time oscillating waveforms, are fitted with numerical results, and the fitting accuracy is acceptable. The frequency of SP is of the order of 10 MHz, and the duty ratio can be tailored from 1 to 0. The tunability of SP, together with the relative low threshold power, may find a variety of potential applications, such as the on-chip distribution of the low-speed optical clock signals. However, when applying a reverse voltage on the PN junction embedded in the MRR, the free-carrier lifetime is reduced by 2 orders of magnitudes, so that the region of SP as well as the stimulating initial condition of SP are all changed, and SP is not observed.

ACKNOWLEDGMENTS

This work was supported by the National Natural Science Foundation of China (grant 60877013).

REFERENCES

- G. Priem, P. Dumon, W. Bogaerts, D. Van Thourhout, G. Morthier, and R. Baets, "Optical bistability and pulsating behaviour in silicon-on-insulator ring resonator structures," Opt. Express 13, 9623–9628 (2005).
- W. H. P. Pernice, M. Li, and H. X. Tang, "Time-domain measurement of optical transport in silicon micro-ring resonators," Opt. Express 18, 18438–18452 (2010).
- 3. L. W. Luo, G. S. Wiederhecker, K. Preston, and M. Lipson, "Power insensitive silicon microring resonators," Opt. Lett. **37**, 590–592 (2012).
- T. J. Johnson, M. Borselli, and O. Painter, "Self-induced optical modulation of the transmission through a high-Q silicon microdisk resonator." Opt. Express 14, 817–831 (2006).
- S. Chen, L. Zhang, Y. Fei, and T. Cao, "Bistability and selfpulsation phenomena in silicon microring resonators based on nonlinear optical effects," Opt. Express 20, 7454–7468 (2012).
- L. Zhang, Y. Fei, T. Cao, Y. Cao, Q. Xu, and S. Chen, "Multibistability and self-pulsation in nonlinear high-Q silicon microring resonators considering thermo-optical effect," Phys. Rev. A 87, 053805 (2013).
- A. E. Fomin, M. L. Gorodetsky, I. S. Grudinin, and V. S. Ilchenko, "Nonstationary nonlinear effects in optical microspheres," J. Opt. Soc. Am. B 22, 459–465 (2005).
- 8. I. S. Grudinin and K. J. Vahala, "Thermal instability of a compound resonator," Opt. Express 17, 14088–14097 (2009).
- T. Y. Liow, K. W. Ang, Q. Fang, J. F. Song, Y. Z. Xiong, M. B. Yu, G. Q. Lo, and D. L. Kwong, "Silicon modulators and germanium photodetectors on SOI: monolithic integration, compatibility, and performance optimization," IEEE J. Sel. Top. Quantum Electron. 16, 307–315 (2010).
- X. Sun, X. Zhang, C. Schuck, and H. X. Tang, "Nonlinear optical effects of ultrahigh-Q silicon photonic nanocavities immersed in superfluid helium," Science Reports 3, 1436 (2013).
- H. A. Haus, M. A. Popovic, M. R. Watts, C. Manolatou, B. E. Little, and S. T. Chu, "Optical resonators and filters," in *Optical Micro*cavities, K. Vahala, ed. (World Scientific, 2004).
- A. de Rossi, M. Lauritano, S. Combrié, Q. V. Tran, and C. Husko, "Interplay of plasma-induced and fast thermal nonlinearities in a GaAs-based photonic crystal nanocavity," Phys. Rev. A 79, 043818 (2009).
- V. Van, T. A. Ibrahim, P. P. Absil, F. G. Johnson, R. Grover, and P.-T. Ho, "Optical signal processing using nonlinear semiconductor microring resonators," IEEE J. Sel. Top. Quantum Electron. 8, 705–713 (2002).
- B. E. Little, S. T. Chu, H. A. Haus, J. Foresi, and J.-P. Laine, "Microring resonator channel dropping filters," J. Lightwave Technol. 15, 998–1005 (1997).
- T. Van Vaerenbergh, M. Fiers, P. Mechet, T. Spuesens, R. Kumar, G. Morthier, B. Schrauwen, J. Dambre, and P. Bienstman, "Cascadable excitability in microrings," Opt. Express 20, 20292–20308 (2012).
- T. Van Vaerenbergh, M. Fiers, J. Dambre, and P. Bienstman, "Simplified description of self-pulsation and excitability by

- thermal and free-carrier effects in semiconductor microcavities," Phys. Rev. A $\bf 86$, 063808 (2012).
- D. Dimitropoulos, R. Jhaveri, R. Claps, J. C. S. Woo, and B. Jalali, "Lifetime of photogenerated carriers in silicon-on-insulator rib waveguides," Appl. Phys. Lett. 86, 071115 (2005).
- S. Park, K. Yamada, T. Tsuchizawa, T. Watanabe, H. Shinojima, H. Nishi, R. Kou, and S. Itabashi, "Influence of carrier lifetime on performance of silicon p-i-n variable optical attenuators fabricated on submicrometer rib waveguides," Opt. Express 18, 11282–11291 (2010).
- T. Kuwayama, M. Ichimura, and E. Arai, "Interface recombination velocity of silicon-on-insulator wafers measured by microwave reflectance photoconductivity decay method with electric field," Appl. Phys. Lett. 83, 928–930 (2003).
- FIMMWAVE, Photon Design Ltd., http://www.photond.com/ products/fimmwave.htm.
- A. C. Turner-Foster, M. A. Foster, J. S. Levy, C. B. Poitras, R. Salem, A. L. Gaeta, and M. Lipson, "Ultrashort free-carrier lifetime in low-loss silicon nanowaveguides," Opt. Express 18, 3582–3591 (2010).